Journal of Iberian Geology
https://doi.org/10.1007/s41513-018-0078-y

RESEARCH PAPER

Monitoring ephemeral river changes during floods with SfM photogrammetry

Mikel Calle[1] · Petteri Alho[2] · Gerardo Benito[1]

Received: 12 January 2018 / Accepted: 4 July 2018

Abstract

Monitoring detailed topographic changes in rivers is an essential tool for understanding the morpho-sedimentary behavior of rivers. However, as the resolution of topographic reconstruction techniques improves, survey costs and the time consumed increase. In this paper, the emerging Structure from Motion Multi-View Stereo (SfM-MVS), a high resolution but low cost technique, is scrutinized to assess whether it constitutes a viable option for 'change detection' in ephemeral rivers. To that end, three photogrammetric flights were carried out to reconstruct the subsequent digital elevation models (DEMs) and quantify fluvial change caused by two floods in 2015 along a 6.5 km reach in an ephemeral gravel-bed river (Rambla de la Viuda; eastern Spain). The application of SfM-MVS resulted in a maximum point cloud density of 1295.4 pts/m^2 and a DEM resolution of 3.11 cm/pix. Individual flights registered errors of 0.101, 0.171 and 0.083 m. Level of detection (LoD) of DEMs of difference (DoDs), i.e. topographic change detection, resulted in 0.198 and 0.190 between the first and second, and second and third flights respectively. Orthomosaics were also successfully created at a maximum resolution of 2.50 cm/pix. Analysis of the best configuration of SfM-MVS for ephemeral river monitoring indicated that a high overlap of photographs and, therefore, a large number of projections were critical for an efficient workflow and a high-quality model. To ensure model quality and survey efficiency, the following configuration is recommended: (1) overlap index of more than 20 projections, (2) flight distribution at two heights, and (3) the use of ground control points. SfM-MVS topographies and DoDs showed a discontinuous pattern represented by a succession of erosive-depositional sequences. Evolution of one of these sequences has been studied in detail and the legacy of a past mining pit was pointed out to be the principal driver for this morphosedimentary pattern. Change detection quantified a net erosion of (−)3118 m^3 for Flood #1 and a net deposition of (+)787 m^3 for Flood #2, at a 95% confidence. Knickpoint retreat, riverbed lowering and bank erosion were identified as the principal sources of sediment. Analyzing separately each flood highlighted that the mobilization of sediments was not proportional to peak discharges (98 and 80 m^3/s, respectively). Interpretation of this behavior was hypothesized to be produced by the difference in total water volume (32.5 and 7.1 hm^3), longer discharge period (24 and 11 days), different entrainment thresholds of each flood, or a clockwise hysteresis effect in the sediment transport, probably due to varying sediment availability. Thus, it was concluded that SfM-MVS worked especially well for change detection in ephemeral rivers and served as a basis for understanding morphological river patterns associated to floods and human impacts.

Keywords Gravel-bed · Change detection · SfM-MVS · Ephemeral river · Level of detection

Resumen

Para llegar a comprender el comportamiento morfosedimentario de los ríos es necesario realizar un seguimiento detallado de los cambios topográficos que tienen lugar en sus cauces. Sin embargo, cuanto mayor es la resolución de la técnica utilizada para la reconstrucción topográfia, el coste y el tiempo necesario para cubrir una cierta superficie se incrementa. En este trabajo se ha utilizado y comprobado la utilidad de la fotogrametría digital automática (Structure from Motion Multi-View Stereo: SfM-MVS), una técnica que puede alcanzar gran resolución a un bajo coste. Para ello se han llevado a cabo tres vuelos fotográficos para reconstruir el modelo digital de elevaciones (MDE) de un tramo de 6.5 km de la Rambla de la Viuda, un río efímero situado en el Levante español. Estos MDE fueron comparados entre sí para cuantificar las modificaciones producidas por dos inundaciones ocurridas en 2015. Se obtuvo una nube de puntos con una densidad máxima de 1295.4 pts/m^2

Extended author information available on the last page of the article

Published online: 12 July 2018

y una resolución para el MDE de 3.11 cm/pixel. Los errores asociados a las tres topografías fueron de 0.101, 0.171 y 0.083 m, respectivamente. El nivel de detección de cambios (LoD) fue de ±0.198 y ±0.190 para los modelos digitales de las diferencias entre las superficies (DoDs), obtenidos entre el primero y el segundo, y el segundo y el tercer vuelo respectivamente. Como subproducto del procesamiento de las topografías se obtuvieron ortofotos con una resolución máxima de 2.50 cm/pix. En relación a la metodología se observó que para un flujo de trabajo eficiente y una reproducción topográfica fidedigna es crucial seguir estas recomendaciones: (1) mantener un alto grado de superposición entre fotografías, manteniendo un valor de número de proyecciones superior a 20, (2) distribuir el plan de vuelo en dos pasadas a dos alturas distintas, para ganar resolución a la par que superposición y (3) el uso de puntos de control fijos al sustrato rocoso, para evitar la gran inversión de tiempo que supone desplegar los puntos de control en el campo. Desde un punto de vista geomorfológico, el resultado de los DoDs reveló la presencia de un patrón discontinuo compuesto por una sucesión de secuencias de erosión-deposito. Una de estas secuencias fue estudiada en detalle desvelando que la aparición, evolución de estas secuencias y su distribución a lo largo del cauce está íntimamente relacionada con la extracción de gravas. Los volúmenes netos de sedimentos movilizados por cada uno de los eventos revelaron un comportamiento muy distinto entre los eventos. La primera inundación (Flood #1) produjo una erosión neta de (−)3118 m^3 mientras que el segundo evento de inundación (Flood #2) produjo una acumulación de (+)787 m^3 ambos calculados dentro del margen de confianza del 95%. Según los DoDs y las ortofotos, las principales fuentes de removilización de sedimento estuvieron asociadas a la erosión del lecho y los márgenes. Hecho que fue aparentemente desencadenado por la migración aguas arriba del knickpoint generado por la extracción de gravas. Analizando por separado cada uno de los eventos de inundación (con picos de 98 y 80 m^3/s, respectivamente) se vio que la respuesta sedimentaria no fue proporcional a su magnitud. Este comportamiento puede estar relacionado con los diferentes volúmenes de agua aportados (32.5 y 7.1 hm^3), diferencias en la duración del hidrograma (24 y 11 días), diferentes umbrales de transporte de cada inundación o a fenómenos de histéresis en sentido horario del transporte asociado a la disponibilidad sedimentaria. Este trabajo concluye que la fotogrametría digital automática (SfM-MVS) funciona especialmente bien para la detección de cambios en ríos efímeros dada su escasa vegetación y ausencia de agua. De esta manera, puede ser una herramienta propicia para comprender los patrones morfológicos asociados a las inundaciones y a los impactos humanos sobre los cauces.

Palabras clave Lecho de gravas · Detección de cambios geomorfológicos · SFM-MVS · Río efímero · Nivel de detección

1 Introduction

Rivers and streams are ubiquitous landforms that play a fundamental role in the conservation of the natural environment. The analysis of river behavior is critical to maintain and guarantee water resources, power generation, recreation, animals and ecosystems (Knighton 1998). Despite the high natural value and ecosystem services provided by rivers, human activities such dam construction, flood risk prevention measures, river lining, water withdrawal, or instream mining, have frequently constituted a source of severe change (Boix-Fayos et al. 2007; Ollero et al. 2015; Rinaldi et al. 2005; Sanchis-Ibor et al. 2017), which, in turn, lead to serious modifications of fluvial and sediment dynamics (Dufour et al. 2015; Kondolf 1994b). Increasing concern over these problems has led to the development of new techniques for assessing ecological, hydrological and geomorphological problems of rivers (Gallart et al. 2012, 2017; Ollero et al. 2015; Stubbington et al. 2018). Identification of these latter is especially important in non-perennial rivers, i.e. cease to flow for some time of the year, where biological and hydrological indicators are not applicable and riverbed morphology is the only remnant after the cease of the flow. In addition, these geomorphological techniques may be relevant considering that non-perennial rivers cover more than 50% of the global river network, and even more in the Mediterranean Europe (Skoulikidis et al. 2017).

Therefore identification of morphological changes and river pattern modifications has been recently used as an alternative for evaluating river conditions (Calle et al. 2017; Sanchis-Ibor et al. 2017). In this respect, 'change detection', "the process of identifying differences in the state of an object or phenomenon by observing it at different times" (Singh 1989), has constituted the basic technique for quantifying changes since the early 1980s (Lu et al. 2007). The preferential use of topographic data (Digital Elevation Models: DEMs), as a precise way of quantify volumetric 'change detection', has driven the development of a suite of techniques for topographic reconstruction, i.e. systematic and non-systematic GPS-based topographies (Brasington et al., 2000; Calle et al. 2015), dense terrestrial laser scanning (TLS) topographic point cloud reconstruction (Brasington et al. 2012), airborne laser scanning (ALS) (Charlton et al. 2003), mobile laser scanning (MLS) with several mounts (Alho et al. 2009; Alho et al. 2011; Flener et al. 2013; Lotsari et al. 2014; Vaaja et al. 2011), as well as classic (Lane et al. 1994) and automated photogrammetry (Javernick et al. 2014; Marteau et al. 2017b). Development of these techniques has increased the accuracy and resolution of the topographic techniques. However, it has also resulted in rising

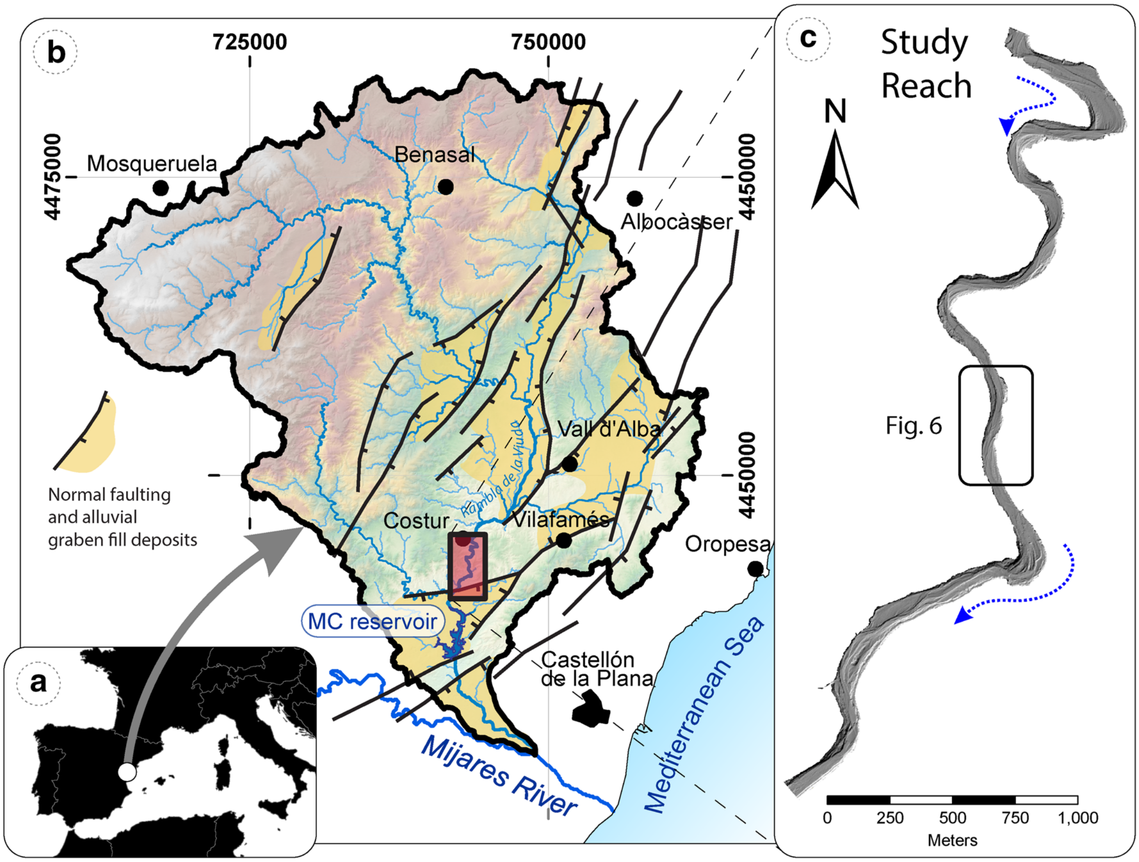

Fig. 1 Rambla de la Viuda study reach (**c**), in the European (**a**), and watershed contexts (**b**)

survey costs, a drawback that is especially exacerbated with repeated high-resolution remote sensing techniques, typically used for 'change detection' (e.g. TLS, MLS, ALS, SAR interferometry).

Combining development of structure from motion technology with Multi-view stereo reconstruction algorithms (SfM-MVS) has helped in solving cost and time issues at a reasonable trade-off between measurement accuracy and point cloud resolution (Verhoeven et al. 2015). SfM methods are based on automated photogrammetry that can reconstruct physical environments from multiple photographs taken from varying viewpoints (camera positions). Camera positioning and orientation are solved automatically and simultaneously from a set of overlapping images without the need to specify internal and external camera parameters (Westoby et al. 2012) by using a highly redundant, iterative bundle adjustment procedure (Snavely 2009).

The potential of SfM-MVS for topographic reconstruction is gaining ground, although limitations in its use for scientific purposes are still being assessed in terms of accuracy, precision and resolution. Recently, a thorough evaluation was conducted of the capabilities and errors derived from SfM algorithms in various software (Fonstad et al. 2013; Javernick et al. 2014; Marteau et al. 2017b; Muñoz-Narciso et al. 2014; Rychkov et al. 2012; Vericat et al. 2009). A general finding for most of the studies is that vegetated environments and the presence of water bodies make good SfM reconstruction difficult. This makes necessary to apply filters, sometimes with questionable results, to eliminate undesirable points related to vegetation and water reflection or refraction effects (Ferreira et al. 2017; Javernick et al. 2014; Nouwakpo et al. 2016).

Despite accuracy tests, good practice in pre-processing and certain guidelines for river surveying are also needed, i.e. evaluation of different flight plans, placement of photo targets or the suitability of filtering under ephemeral conditions. These issues should be further investigated, since they may affect the efficiency and quality of processing photographs and lead to project failures. It will also contribute to establishing good practice for applying SfM-MVS to rivers in general, and ephemerals in particular.

The aims of this paper are: (1) to test different configurations of SfM-MVS methodology for developing accurate riverbed topographic reconstructions, (2) to evaluate the level of detection of SfM-MVS when 'change detection' is applied to ephemeral rivers, (3) to quantify and interpret

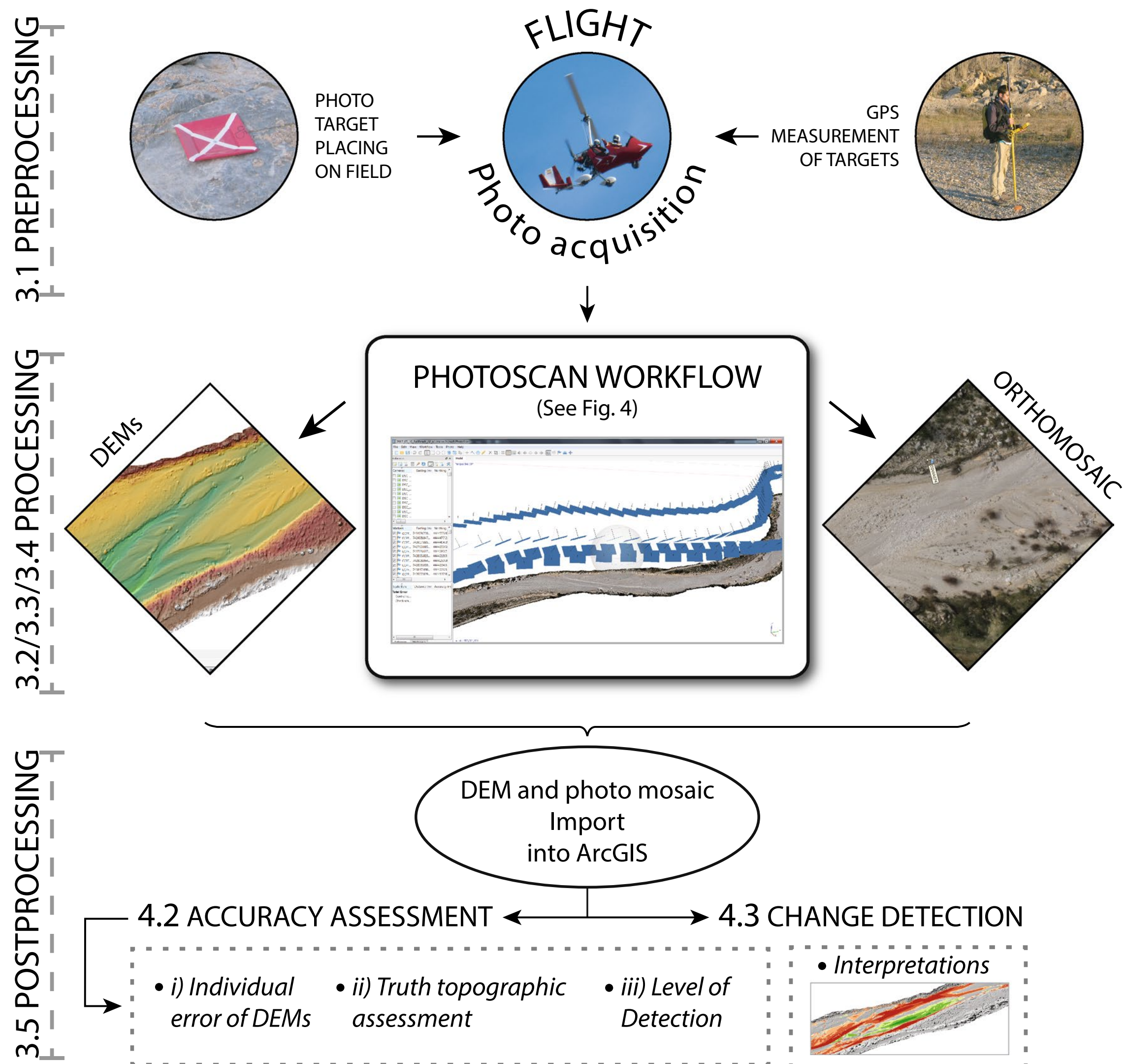

Fig. 2 General workflow of this study

spatio-temporal changes of river bed forms after floods in ephemeral fluvial systems. In order to carry out these tasks, three low-altitude aerial photo sets (February 2015, June 2015 and February 2016) were taken in a 6.5 km long reach of an ephemeral river in the mid-eastern coast of Spain, which enabled changes caused by flooding in March and November, 2015 to be monitored.

2 Study site

The study area comprises a 6.5 km long reach of the Rambla de la Viuda River, an ephemeral river located in the province of Castellón, eastern Spain (Fig. 1). The watershed feeding Rambla de la Viuda covers 1523 km^2 and two main structural domains: the Iberian Chain and Maestrat graben system (Salas and Casas 1993). Their origins relate mostly to Alpine orogeny (compressional, 55–25 Ma) and Valencia Through (extensional, 25–2.5 Ma).

This study focuses on a stretch of the river located in the graben system. The middle fork of Rambla de la Viuda, directly upstream the study reach, flows over the graben system filled with Plio-Pleistocene alluvial conglomerates, lacustrine limestones and marls (Anadón and Moissenet 1996; Simón et al. 2013). Later, the Rambla de la Viuda cuts through a horst structure made of Cretaceous limestones where the study reach is located (Fig. 1). In this section, the river corridor is entrenched and two or three times narrower than in the graben. The upstream geological framework (bedrock + alluvial conglomerates) promotes an abundant supply of gravel to the study area. However, general degradation of the bed and formation of micro-terraces (1–2 m) were caused by gravel mining.

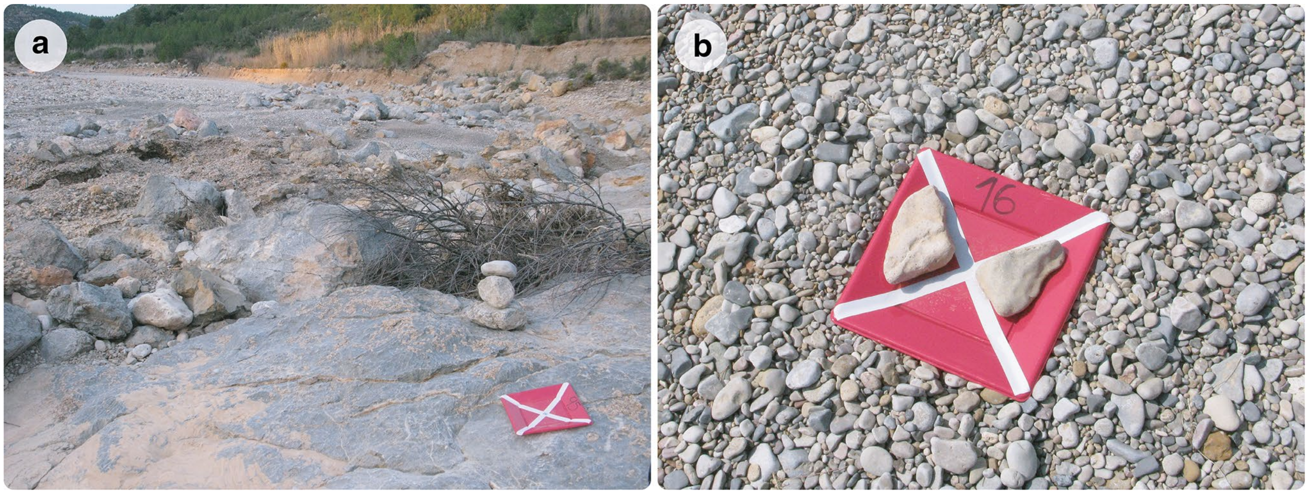

Fig. 3 Example of **a** permanent targets screwed to a rock surface (target in a permanent position in subsequent flights) and **b** mobile targets

Table 1 Principal characteristics of the flights

Name	Date	Flight height (m)	Flight speed (km/h)	No. of pho.	Camera resol. (pix)	Rate (fps)	No. of targets	Distribution	Target type
Flight 1	Feb. 2015	~100	65–83	1440	4000×3000	0.87	143	Rand	M
Flight 2	Jun. 2015	~50	68–80	1535	4000×3000	0.87	138	CS	M
Flight 3	Feb. 2016	~75 and ~150	84–95	1537	6000×4000	1.15	138+67	Rand&CS	P+M

The same area was selected for creating statistics. See Fig. 3 for a representative picture of both target types

Rand Randomly distributed targets, *CS* cross sectional distributed targets, *M* mobile target type, *P* permanent target type, *Rate* the rate of shooting in frames per second

This fluvial reach is entrenched in bedrock, but with an alluvial valley bottom. The average channel gradient is 0.0257 and its width ranges between 30 and 125 m. Gravel sediment size (D50) in active areas was 22.6 mm during the studied period.

The Rambla de la Viuda ephemeral regime is a consequence of the natural rainfall distribution. The mean annual precipitation in the watershed ranges between 450 and 600 mm with an autumn peak. Maximum daily mean discharges, estimated from the volume of water accumulated daily in the Maria Cristina (MC) reservoir, were registered in 1962, 1969, 1989 and 2000 with 659, 238, 286 and 385 m^3/s, respectively (Machado et al. 2017). In the period 1960–2000, the average of events per year was 2–3, with an average flow of 30 days per year (Camarasa-Belmonte and Segura-Beltrán 2001).

3 Methods

3.1 Flight plan

Designing the flight plan is a crucial step in any kind of photogrammetric study, as the selected approach will control the final results. In this research we used the same approach for all three flights (Fig. 2). Aerial photos at low elevation were taken from a two-seater autogyro. Flights were always made on the same day by covering the reach four times, two for each bank. This ensured sufficient overlap of the photographs and increased the variety of angles capturing sharp features. Photo targets were used as Ground Control Points (GCPs) for georeferencing and analyzing the quality of the reconstructed topography. A combination of targets both randomly distributed and focused on cross-sections was selected for the best georeferencing. Photo targets consisted of 25×25 cm red plastic squares with an X marked in 1.5 cm width adhesive white tape from corner to corner (Fig. 3). Target centroids were surveyed using Trimble 4700 GPS in RTK mode to obtain XY coordinates and orthometric

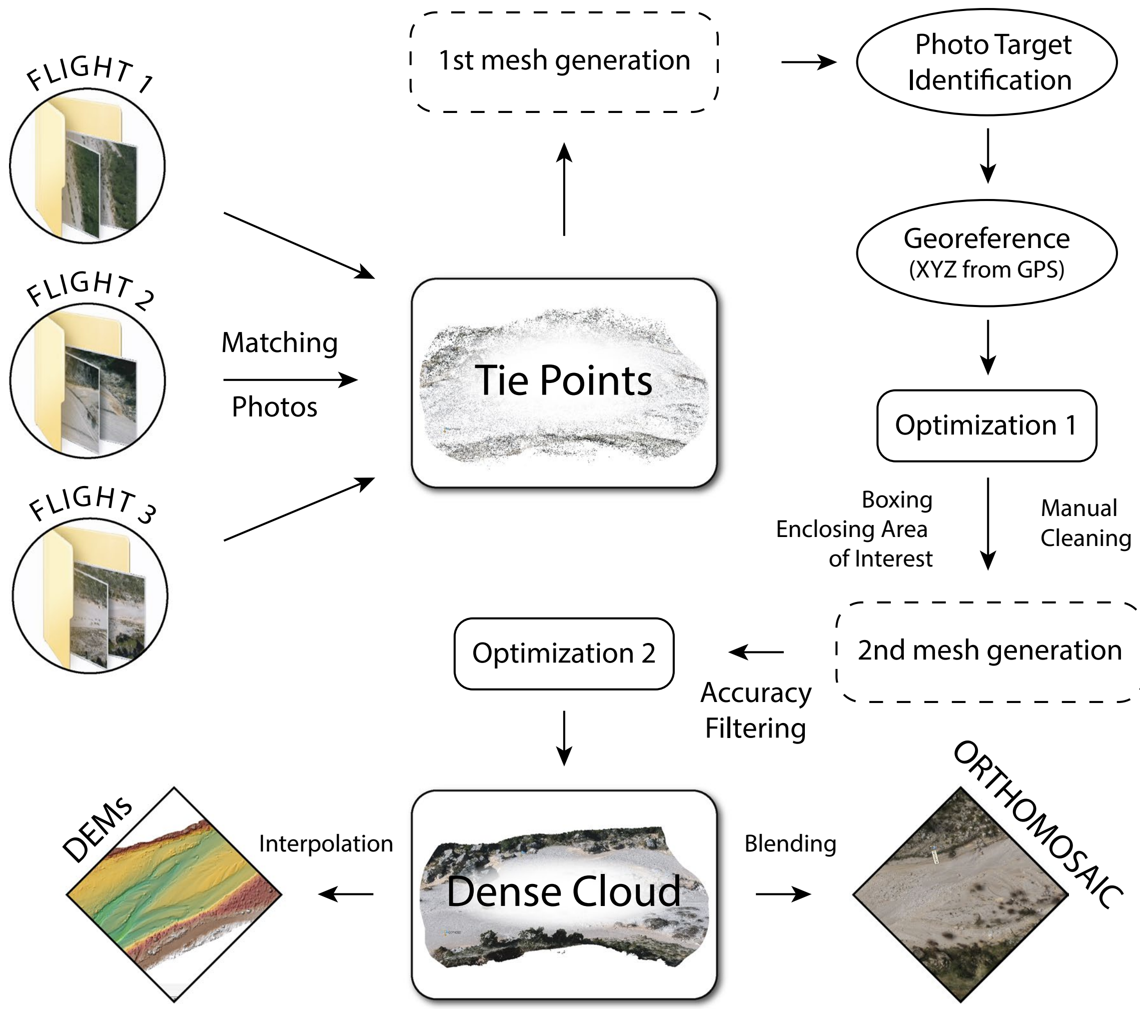

Fig. 4 SfM workflow in PhotoScan leading to DEM and Orthomosaic generation that are the basis for change detection, sediment budget and transfer analysis of this work

heights with errors under 0.02 m in XY and 0.05 m in Z. Coordinates were acquired in WGS84, transformed into ETRS89, and projected into EGM08—REDNAP, the official geoid for Spain. Active trial-and-error enabled some of the described methodological elements for subsequent flights to be modified, such as the location and density of referencing points, camera replacement or flight paths (Table 1).

Flight 1, approximately 100 m above the riverbed, was carried out to act as the reference channel topography for later flights. A compact digital camera (Cannon PowerShot G9) with 12.1 megapixels was used (Table 1). Focal length was set to 7.4 mm (1×), 35 mm equivalent, for minimal image distortion (Javernick et al. 2014). When possible, GCPs were positioned on top of horizontal surfaces mapped as active areas or sparsely vegetated bars (Calle et al. 2017).

Flight 2, approximately 50 m above the riverbed, aimed to detect changes occurring after a large flood in March 2015. The same flight paths and pass-overs were used. However, in this case, the lower height was planned to increase image resolution and thus model accuracy (Table 1). Camera model and settings were the same as in flight 1.

Flight 3 documented changes after a flood that occurred in November, 2015. Despite the good resolution of photographs from the previous flight, overlap was adversely affected by the lower flight elevation. To avoid this problem, the flight was completed at two heights, a lower flight (75 m) to give resolution and a higher one (150 m) to guarantee sufficient overlap (Table 1). The distribution of flight paths was changed to register the same river bank by flying upstream and downstream, and repeating the same procedure on the other bank. Additionally, to increase resolution, the camera was replaced by a 24 megapixels Nikon D5500 (Table 1). Focal length was set at 23 mm (manually adjustable focal lens 18–55 mm) almost a 35 mm full frame equivalent.

During this flight, permanent targets were introduced (Fig. 3a). The square targets were drilled and screwed into

Table 2 Parameters used for the final computations for the entire reach and on each flight

Step	Parameter	Selected parameter
Alignment	Accuracy	High
	Pair pre-selection	Generic
	Key point limit	0
	Tie point limit	0
	Constrain features by mask	Yes-2nd mesh
Tie point cloud	Optimization	Yes
	Parameters	f, b1, b2, cx, cy, k1-k4, p1, p2
Reconstruction parameters	Quality	High
	Filtering	Mild
DEM	Interpolation method	Height field
Orthomosaic	Blending mode	Mosaic
	Surface	DEM
	Color correction	Yes

rocky surfaces or boulders that potentially remain on site after flooding, in order to greatly reduce the amount of time spent placing the GCPs in future campaigns.

3.2 The software

One of the SfM-MVS programs on the market is PhotoScan (Agisoft 2016b), which has intuitive interface and powerful algorithm to provide effective results and an accurate topographic reconstruction when combined with Ground Control Points (GCPs). This software has been previously used for river topography reconstruction, e.g. Javernick et al. (2014), Marteau et al. (2017a); Muñoz-Narciso et al. (2014) and Smith et al. (2014) with encouraging results.

3.3 PhotoScan workflow

The principal advantage of SfM is that it is a fully automated photogrammetric method that can reconstruct 3D environments. When coupled with a Multi View Stereo (MVS) algorithms, it is capable of producing high-resolution DEMs that fall between ALS and TLS (Doneus et al. 2011; Fonstad et al. 2013; Javernick et al. 2014).

SfM-MVS workflow for 'change detection' comprises three main stages (Fig. 4): (a) SfM algorithms utilize photographs to create a 'tie point' or 'sparse cloud'. Output from this process determines camera position and internal and external orientation parameters (Javernick et al. 2014). (b) Building up a 'dense cloud', where every pixel is used to vastly increase scene details by applying MV3D reconstruction algorithms (Verhoeven 2011). (c) Scaling and/or referencing the model. In topographic reconstruction, photo targets spread over the area of interest are used as ground control points (GCPs) to add XYZ coordinates. More details about photogrammetric processing can be found in Doneus et al. (2011), Fonstad et al. (2013), Javernick et al. (2014) and Verhoeven et al. (2015).

Testing parameter functions is tedious, but at the same time essential for selecting the best options for software performance (Javernick et al. 2014). In order to make an effective assessment of adequate parameters to deal with the entire dataset, a 500 m long reach was selected comprising ~ 150 photographs and 8–10 visible targets. This small area enabled rapid evaluation of the SfM workflow to obtain the best parameters for the final processing (Table 2). Moreover, this step defined the best workflow for processing data for ephemeral rivers (Fig. 4).

In addition to the preliminary parameter tests over the small area, dividing the study section may also increase processing efficiency. According to Agisoft (2016a) user manuals, the software is able to process point clouds and modeling at 'High Quality' and 'Field Height' mode, appropriate for aerial imagery, with about 500 photos (Agisoft 2016a; Javernick et al. 2014; Verhoeven 2011). Therefore, the study reach was split into three segments (sub-reaches), each approximately 3 km long, and 500 photos taken for efficient dataset processing and editing. After completing the workflow for each segment, they were merged for further analyzing as a single model.

3.4 DEM generation

No vegetation filtering was used prior to DEM generation. According to results shown in Javernick et al. (2014), filtering algorithms reduced errors in vegetated areas, but produced negatively biased results from bare surfaces. In this study, we decided not to filter point clouds as most of the areas were bare gravel surfaces. Exclusion of vegetated banks and isolation of active areas by polygon cut was applied, which was sufficient to avoid the filtering issue, with promising results.

DEM generation was performed with PhotoScan's "Build DEM" option. The interpolation method was unspecified, and was left at the maximum resolution for DEM generation. The 'Interpolation method' (Agisoft 2016a) and a resolution of 0.25 m/pixel was used for DEM exportation into ArcGIS. This homogenized the topographies and enabled a comparison of flights of the same scale. The fact that no vegetation filters were used allowed direct assessment of the accuracy of PhotoScan's interpolation algorithms. Using DEMs and avoiding exports and filtering extremely large point cloud files decreased post-processing times, by boosting and facilitating the use of the data.

3.5 Change detection

The DEM of difference (DoD), the final 'change detection' results, were carried out entirely in ArcGIS. DoDs were obtained by subtracting the final topography out of the previous topography for the same area (Alho et al. 2011; Kasvi et al. 2013; Lotsari et al. 2014). A polygon was used to mark out the widest 'active area' of the three flights and exclude areas without changes. The same polygon was used for the whole period, i.e. the three flights, to maintain boundaries for change detection. In addition, DoDs were created with the same spacing as the input DEMs (0.25 × 0.25 m) starting from a specific point, so that the grid cells were fully coincident.

3.6 Accuracy assessment

Evaluation of errors prior to interpretation is recommended. The main goal of an individual quality assessment of DEMs is to provide an overview of the geometric representativeness of the reconstructed surfaces. In this case, a number of GCPs representing an (estimated) real location, were used to obtain the georeferenced surface. As in normal procedure, 2/3 of the GCPs were used as control and the rest as check points [bootstrapping, e.g. Javernick et al. (2014), Muñoz-Narciso et al. (2014) and Vericat et al. (2009b)]. The remaining GCPs were used for surface quality evaluation (ground truthing) by comparing DEM surface heights and 'true' GPS locations.

Statistics were computed by exporting and calculating residual values of XYZ produced by subtracting PhotoScan's

Table 3 Workflow results for the three flights

Name	Number of points	Point density (pts/m^2)	DEM resolution (cm/pix)	Mosaic resolution (cm/pix)	Overlap index (mean num. projections)
Flight 1	382,041,610	515.8	5.58	2.79	21
Flight 2	550,031,931	742.5	5.00	1.55	11
Flight 3	959,578,113	1295.4	3.11	2.50	29

Table 4 Errors in XYZ directions (Dir.) and 3D of the control points in georeferencing

Data	*n*	Dir.	Pr 95% (|T| > |t|)	RMSE	ME	Min	Max	SD
Flight 1 (F1) **5 outliers*								
C	95	x	0.4477	0.164	−0.025	−0.271	0.405	0.129
C	95	y	0.4088	0.137	−0.009	−0.290	0.498	0.128
C	95	z	0.6215	0.242	−0.028	−0.563	0.533	0.209
C	95	3D Error	0.039	0.689	0.834	0.277	0.834	95
Flight 2 (F2) **2 outliers*								
C	94	x	0.5990	0.111	−0.003	−0.189	0.236	0.056
C	94	y	0.5237	0.056	−0.004	−0.190	0.179	0.053
C	94	z	0.8841	0.052	−0.001	−0.201	0.149	0.050
C	94	3D Error			0.005	0.335	0.332	0.092
Flight 3 (F3) *1*outlier*								
C	126	x	0.885	0.074	−0.001	−0.332	0.207	0.073
C	126	y	0.786	0.688	0.002	−0.169	0.270	0.069
C	126	z	0.667	0.057	0.002	−0.097	0.199	0.048
C	126	3D Error			0.005	0.430	0.427	0.111

All measurements are expressed in meters. Null hypothesis, Pr 95% (|T| > |t|), was calculated for 95% probability estimated values and supplied RTK-GPS coordinates. In addition, Student's *t* test was carried out on the points to validate the null hypothesis (Pr 95%, |T| > |t|) and evaluate the occurrence of any systematic error. As suggested by Javernick et al. (2014), root mean square error (RMSE) was used to measure surface quality, mean error (ME) for accuracy, and standard deviations (SD) for precision. In addition, 3D errors were calculated to measure 3D accuracy.

DEM comparisons require identification of the thresholds of change detection, which clarify whether a change is due to noise or caused by a real topographic change (Wheaton et al. 2010). To evaluate this 'Level of Detection' (LoD), the

Table 5 Check points and 'ground truthing' errors

Check	Obs	Pr 95% (|T| > |t|)	RMSE	ME	Min	Max	SD	68% (±)	95% (±)
F1	42	0.099	0.051	0.013	−0.122	0.207	0.050	0.050	**0.101**
F2	53	0.634	0.111	0.006	−0.377	0.254	0.085	0.085	**0.171**
F3	62	0.000	0.096	−0.020	−0.120	0.067	0.041	0.041	**0.083**

No outliers were excluded in calculations in Flight 1, one outlier was excluded in Flights 2 and 3. Null hypothesis, Pr (|T| > |t|), was calculated for 95% probability

Bold numbers highlight the values used for estimating the level of detection

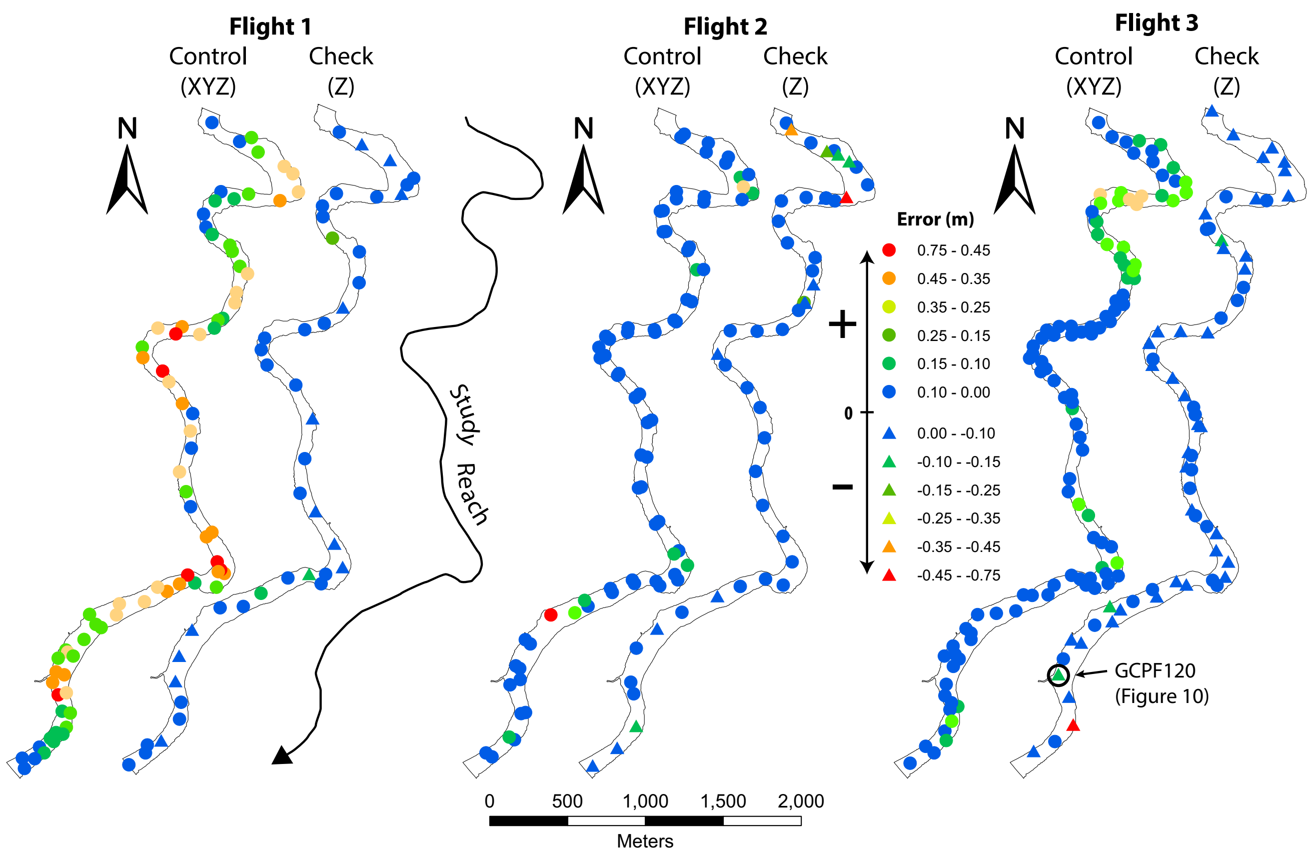

Fig. 5 RMSE distribution along the model for the three flights. Control points used for georeferencing are on the left, and the 'Ground truthing' error distribution of check points is on the right

Table 6 Propagated uncertainties in Z dimension at 68 and 95% confidence intervals for DoDs calculated from combinations of F2–F1, F3–F2 and the whole period, F3–F1

DoD	Dir.	δz_{post} 68% conf (±)	δz_{pre} 68% conf (±)	δu_{DoD} 68% conf (±)	δz_{post} 95% conf (±)	δz_{pre} 95% conf (±)	δu_{DoD} 95% conf (±)
F2–F1	z	0.085	0.050	0.099	0.171	0.101	**0.198**
F3–F2	z	0.041	0.085	0.095	0.083	0.171	**0.190**

Bold number indicates the LoD used for calculations

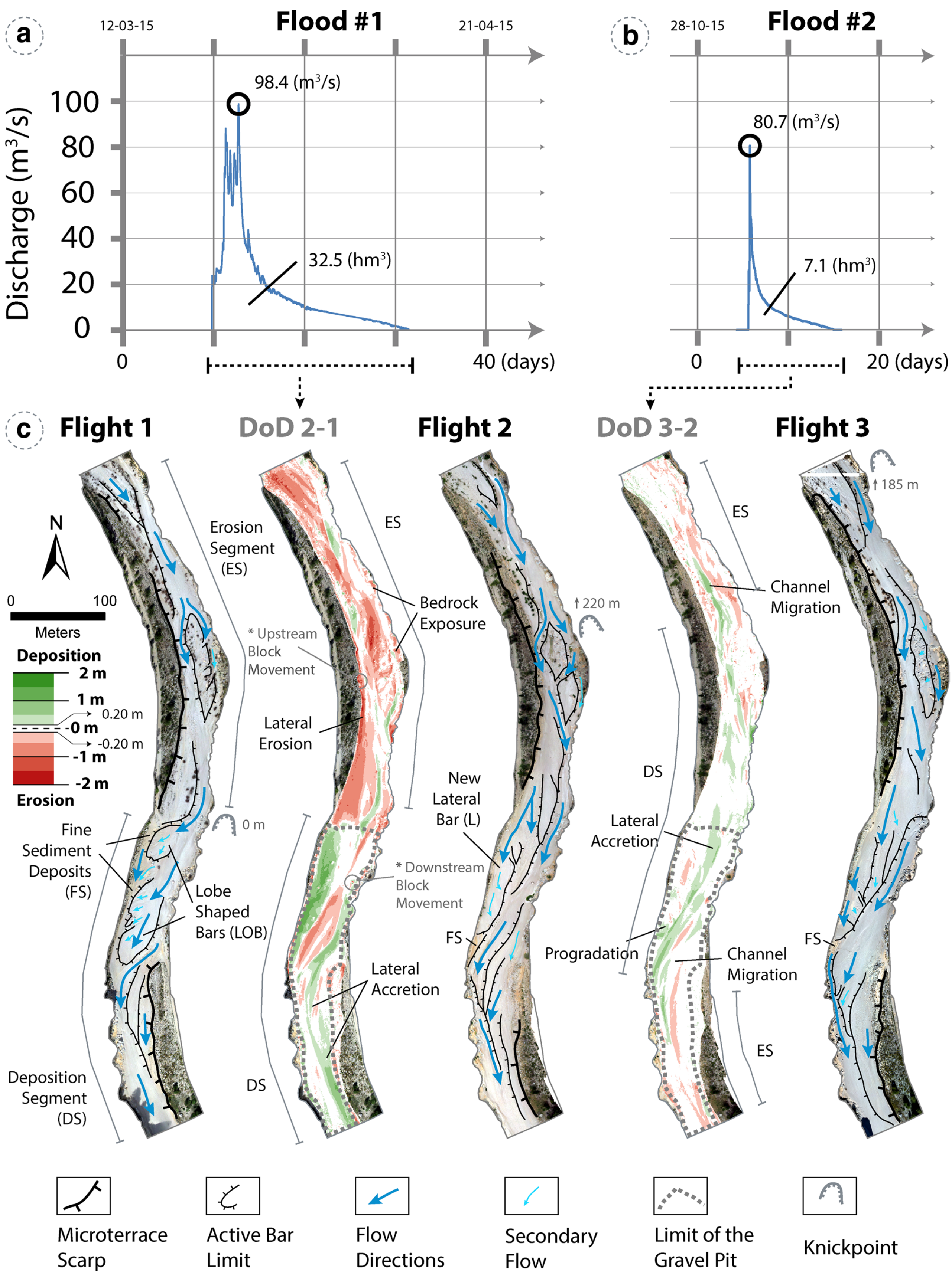
a
Flood #1
12-03-15
21-04-15
Discharge (m³/s)
100
80
60
40
20
0
98.4 (m³/s)
32.5 (hm³)
0
40 (days)
b
Flood #2
28-10-15
80.7 (m³/s)
7.1 (hm³)
0
20 (days)
c
Flight 1
DoD 2-1
Flight 2
DoD 3-2
Flight 3
N
0
100
Meters
Deposition
2 m
1 m
0.20 m
0 m
-0.20 m
-1 m
-2 m
Erosion
Erosion Segment (ES)
Fine Sediment Deposits (FS)
Lobe Shaped Bars (LOB)
Deposition Segment (DS)
0 m
* Upstream Block Movement
Lateral Erosion
Bedrock Exposure
ES
DS
* Downstream Block Movement
Lateral Accretion
New Lateral Bar (L)
FS
220 m
Channel Migration
Lateral Accretion
Progradation
Channel Migration
185 m
Microterrace Scarp
Active Bar Limit
Flow Directions
Secondary Flow
Limit of the Gravel Pit
Knickpoint

◂**Fig. 6** Hydrographs of the Flood #1 (**a**) and Flood #2 (**b**). Orthomosaics and DoDs of the detail study area (**c**). Flight orthomosaics represent the morphological conditions between events while DoDs show the detailed morphological change caused by the floods

following equation was used to express a general uncertainty value for the entire DoD:

$$\delta u_{DoD} = \sqrt{(\delta z_{post})^2 + (\delta z_{pre})^2}, \quad (1)$$

where δu_{DoD} is the propagated uncertainty in the DoD comparing δz_{post} and δz_{pre}, the individual uncertainties of post-flood DEM and pre-flood DEM, respectively. δu_{DoD} at a 95% confidence interval was used as the threshold of significance or level of detection. Areas below this Level of Detection (LoD) are then considered as noise, and areas above are, therefore, used for volume calculations. The exclusion of noise was achieved by masking DoD pixels below the value of δu_{DoD} in both negative and positive signs.

4 Results

4.1 Point clouds, DEMs and orthomosaics

The primary result of the Photoscan workflow was the dense point cloud generation (see Sect. 3.3). Flight 3 campaign resulted in the densest point cloud out of the three flights. Point cloud conversion into DEMs, before exporting into ArcGIS, resulted in a maximum resolution of 3.11 cm/pix in Flight 3. Maximum resolution of orthomosaics was achieved in Flight 2 with 1.55 cm/pix. Detailed characteristics of the point clouds, and DEMs and orthomosaic resolutions can be seen in Table 3.

Homogenized DEMs (0.25×0.25 m pixel) were exported and compared to characterize the geomorphic effectiveness of flow magnitude in both events. Orthomosaics were also imported into ArcGIS to assist the morphological interpretation of changes.

4.2 Accuracy assessment results and level of detection

After the surface topographic reconstruction with SfM-MVS, and before interpreting river changes, the accuracy results of the method had to be checked. The purpose of this section is to determine whether the changes obtained by this method are ‘true’ topographic changes or not, i.e. above or below the Level of Detection (LoD) at 95% confidence.

Table 4 summarizes the results obtained for the three flights, and shows how null hypothesis, i.e. XYZ mean errors is significantly close to 0 value, is rejected in all control points (Pr 95%, $|T| > |t|$). The remaining GCPs were used for surface quality evaluation (ground trothing, also known as check points) by comparing DEM surface heights and ‘true’ GPS locations (Table 5). This evaluates how close the final topography of the DEM is to the real surface of the river in the Z direction. Check points of Flight 3 suggested that the null hypothesis was not rejected and indicated a negative bias. The value of two standard deviations (95% confidence interval) was included for measuring the individual DEM error. Spatial distribution of individual and ground truth errors along the reach can be seen in Fig. 5, ‘Control’ and ‘Check’ maps, respectively.

Individual DEMs errors are then used for estimating each LoD, i.e. by using Eq. (1) and individual uncertainties of post-flood DEM and pre-flood DEM, respectively. Results at 68 and 95% confidence intervals are shown in Table 6. Values of LoD at a 95% confidence interval (0.198 and 0.190 m) have been included for interpreting changes. In this case the round number of 0.20 (instead of 0.198) has been used for excluding changes from −0.20 to 0.20 m in DoDs.

4.3 Change detection of consecutive flood events

Detailed evolution of changes was analyzed in a reduced area of the studied reach to highlight small scale processes (Fig. 1, Section A). This area constituted an active in-channel gravel extraction area from 2009-2012 (dotted line in Fig. 6). The two flow events under study were used to infer the effects of flood magnitude under the previous conditions i.e. gravel mining. It should be noted that, due to its ephemeral nature, studying the pre- and post-event DEMs of floods provides a continuous archive of the riverbed morphology (Fig. 6).

The initial conditions (Fig. 6, b; Flight 1) consist of two areas of ca. 400 m long each with different behavior: a predominantly erosion segment (EA in Fig. 6) and an associated downstream deposition segment (DA). In EA, river banks, microterraces and bars evidenced active erosion. EA is followed downstream by a development of lobe shaped bars (LOB) where most sedimentation occurs. Some ‘erratic’ boulders leftover from mining, 2.5 m maximum size, are found in this segment (Fig. 7).

‘Flood #1’ was studied by comparing ‘Flight 2’ and ‘Flight 1’. The hydrograph recorded at 5 min intervals provided a peak discharge of 98 m^3s^{-1}, total volume of 32.5 hm^3 and 24 days of streamflow (Fig. 6a). Lateral erosion of old cemented gravel (microterraces) and degradation of the riverbed by knickpoint migration were the principal changes observed in segment EA (Fig. 6). As a consequence, block, bedrock and older cemented gravel were exhumed in this upper part (Fig. 7b). The maximum channel surface erosion was 2.20 m due to lateral erosion, and the channel bed

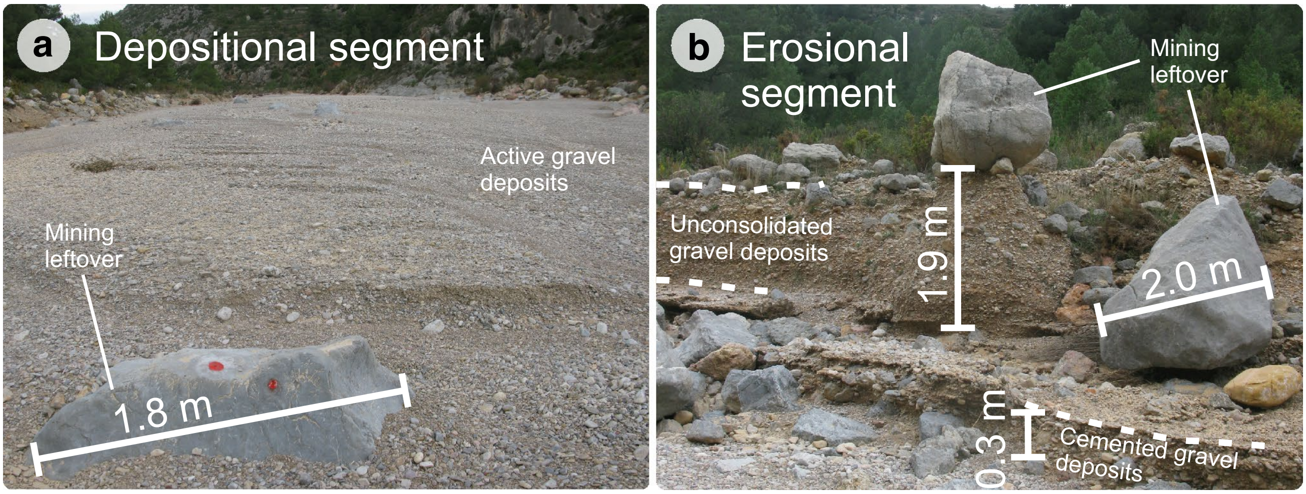

Fig. 7 Example of erratic boulders left by mining in the studied reach after Flood #2. **a** Boulders over the river channel in a depositional segment and **b** boulders over a microterrace in an erosive segment. In the first one, boulders that were previously exposed are being covered by lobe progradation, downstream of the knickpoint (DA in Fig. 6, Flight 1). In the second one, upstream of the knickpoint (EA in Fig. 6, Flight 2), boulders are completely exposed. About 2.2 m (1.9 + 0.3 m) was incised since mining left the boulder at the valley bottom

Table 7 Volumetric 'change detection' at the study section

Compared flights	Subreach	Process	Active area (m^2)	Volume (m^3)	Net vol. (m^3)	Average change (m)
F2–F1	EA	Dep.	966	404	**−4654**	−0.47
		Ero.	8984	5058		
	DA	Dep.	5062	2837	**1536**	0.19
		Ero.	2875	1301		
F3–F2	EA	Dep.	1908	742	**158**	0.04
		Ero.	1748	584		
	DA	Dep.	2717	987	**629**	0.16
		Ero.	1149	358		

Flights are named F1, F2, and F3. The 'area' column represents the total surface affected by sedimentation (Sed.) or erosion (Ero.). 'Net volume' represents the final balance of sediment in the studied section

Bold highlight values discussed in the text

was lowered by 1.65 m. The net volume loss (accumulation minus erosion) in this segment was 4654 m^3.

Downstream, in the DA segment, lateral accretion and longitudinal bar growth were the main phenomena observed. The lobe shaped bars were reworked, and a new lateral bar (L) was deposited with a well-developed longitudinal sorting. Movement of a metric-scale boulder (BM in Fig. 6b) was also detected on the left margin of the area. The maximum channel surface aggradation was 1.50 m of gravel accumulation due to progradation of lobe-shape bars towards the accommodation space left by mining (FS area in Fig. 7b). The volume gained in this DA segment was 1536 m^3. A total exported gravel volume of 3118 m^3 (from erosion) for the entire reach was estimated for 'Flood #1' (calculated from Table 7).

'Flood #2' was studied by comparing Flight 3 and Flight 2 and characterized by a 5 min interval peak discharge of 80 m^3s^{-1}, a total volume of 7.1 hm^3 and 11 days of continuous streamflow. This time, erosive and sedimentation zones shifted upstream (following knickpoint migration) redistributing the previously defined segments (EA and DA) showing a new pattern. Maximum aggradation in segment EA was 1.00 m of bar formation. Erosion was also significant with a maximum of 0.75 m, due to channel incision. The volume surplus in this segment was 158 m^3.

The maximum deposition in the DA segment was 0.80 m of gravel from lateral migration of bars and channel aggradation. The average surplus volume for the segment was 629 m^3 and therefore, the total volume of deposited gravel was estimated at 787 m^3 (from upstream inputs) resulted from 'Flood #2' (calculated from Table 7).

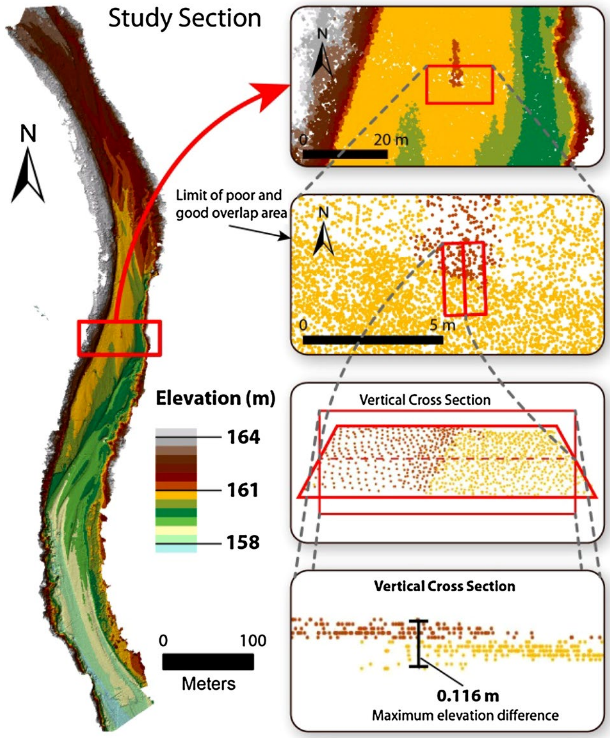

Fig. 8 Poorly overlapped areas in the study site caused 'spatial' or 'model continuity' breaks within the Flight 2 point cloud. An insufficient number of projections or overlap between adjacent photographs causes decimetric scale breaks (bottom right). Please note that the area shown is the same as Fig. 6, that is also represented in Fig. 1 by 'Fig. 6' box

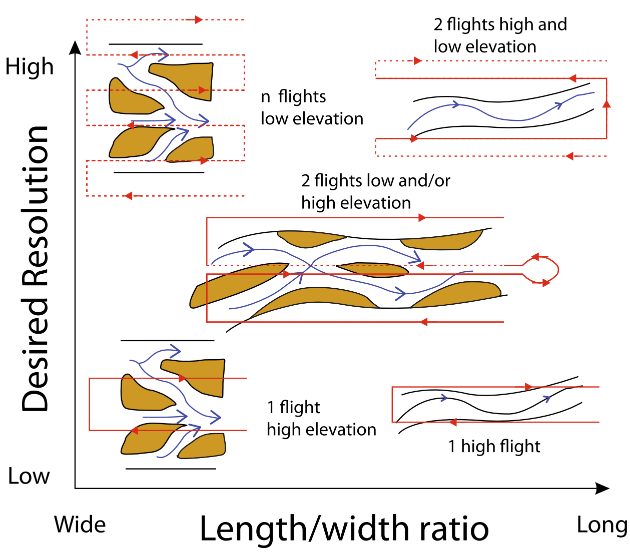

Fig. 9 Flight path recommendations depending on the resolution and length/width ratio of the studied river reach. Dotted lines represent lower elevation flights (above the riverbed)

5 Discussion

This project provides new improvements in SfM-MVS surveying and preprocessing workflow while demonstrating the capabilities of this technique for ephemeral fluvial studies.

5.1 The essentials for photogrammetric river surveying

Despite good results, all that glitters is not gold. Lessons learned during this study highlighted certain issues regarding 'good practice' for SfM-MVS that must be borne in mind to reduce future failures and inefficiencies in the SfM-MVS workflow. The Overlap Index showed in Table 3, i.e. the number of projections, is a measure of the number of times that a physical object is captured by a photograph. It constituted a very influential variable for this study and also for other SfM-MVS projects (e.g. Luhmann et al., 2013). This number may be understood as a measure of model consistency ("unbroken") and quality throughout the entire model. Unfortunately, the accuracy assessment used in most studies (Vericat et al. 2009b; Wheaton et al. 2010; among others) is unable to detect these issues. Thereby, a reduced number of projections would result in lower quality of the model that may not affect the individual accuracy assessment results. An example of these 'spatial' or 'model continuity' anomalies is Fig. 8, where low photograph overlapping produced a bulge that breaks the continuity of the model. This is reflected in Table 3 that showed an overlap index of 11 for Flight 2 in contrast to the value of 21 for Flight 1. Interestingly, Flight 2 had lower value of ME than Flight 1 (Table 5). In this situation, if quality assessment for the model is only aware of errors, these 'model continuity' problems could be overlooked. Thus, the number of projections may also be included as a model quality indicator that we recommended to remain above a value of 20 for long SfM-MVS river surveys (reference values achieved in Flights 1 and 3 which proved to have good 'model continuity').

This insufficient overlap caused difficulties, not only in the final product, but also at alignment stages, resulting in a vast increase of editing time and many failed attempts that led to a less efficient workflow. Therefore, in addition to accuracy, reconstruction efficiency was directly proportional to the overlap of photographs and number of projections of physical points (Fonstad et al. 2013).

This must be the focus when designing a photogrammetric field campaign. If, for example, increased resolution is desired, two recommendations could be made in order not to affect overlap:

It is highly advisable to increase camera resolution (changed in Flight 3) instead of decreasing flight height (changed in Flight 2). At a given speed, the lower the flight,

Table 8 Target type test

Type of targets	Obs	Pr 95% (|T| > |t|)	RMSE	ME	Min	Max	SD
GCPM	19	0.3751	0.021	0.004	−0.031	0.052	0.021
GCPF	30	0.0070	0.046	−0.022	−0.131	0.038	0.042

Associated errors and null hypothesis (95% probability) for the check points of Flight 3

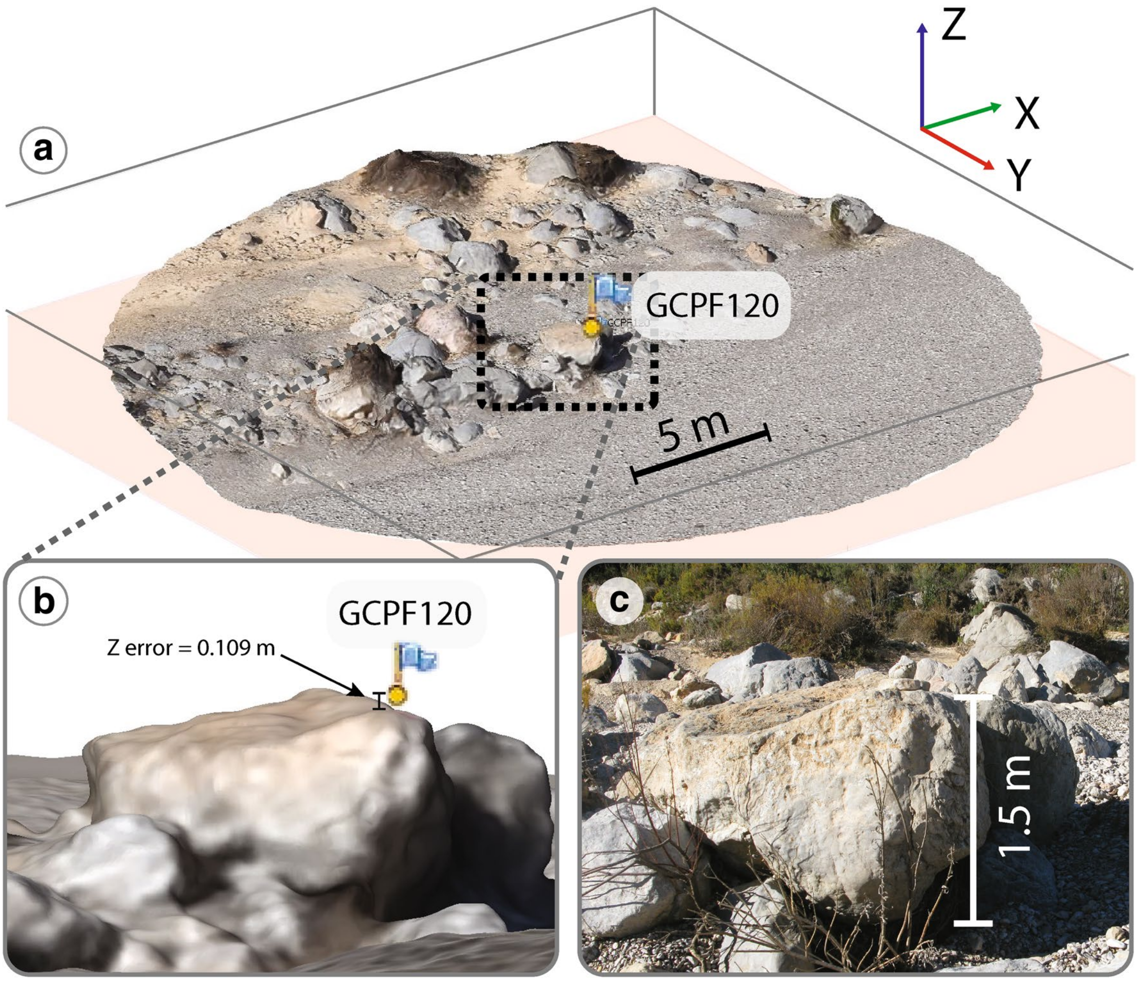

Fig. 10 Example of underestimated elevation at GCPF120: **a** DEM of the surrounding area of GCPF120 (texture on); **b** detailed view of the model pointing out the underestimated height at the edge of the boulder where the target is drilled; and **c** field photograph of the boulder. GCPF120 is referenced in Fig. 5, Flight 3, Check points. Please note that this was the second higher underestimation of the study. Others were significantly lower (cm scale)

the less overlap of photographs. In our case, flight speed cannot be set under a certain level owing to the autogyro lift mechanism, and flight height is the only parameter that is customizable when the camera is set to shoot at maximum rate.

At the time of planning flight paths, we propose distribution depending on the length/width ratio of the study reach (Fig. 9). In our case (ratio 70:1 and high resolution), the distribution of flight paths at high and low elevations resulted in a better overlap without compromising accuracy and model continuity. The higher flight path was able to ensure good overlap, while lower flights increased image and thus topographic resolution. In addition, more oblique angles obtained by flying low and over the banks enhanced capturing sharp and steep features.

Furthermore, in order to save time in the future while deploying targets before the survey, the use of permanent targets was tested in Flight 3. These corresponded to fixed targets on hard surfaces (GCPF) that can be included as targets in future surveys. They may save time when positioning targets over large areas and may also provide a measure of consistency between surveys when compared. However, ME in Table 5 did not refute the Null Hypothesis 'Pr (|T| > |t|)'. When tracking the underestimation of 0.02 m in height, we detected that the GCPFs were responsible for the deviation (see ME for GCPF in Table 8). There is no clear explanation for this phenomenon, but it is suspected that may be due to GCPF placement. GCPFs with higher error values corresponded to targets drilled too close to steep edges of blocks. In these conditions, the topographic model may have slightly underestimated point height (e.g. Fig. 10, where underestimation of 0.109 m was encountered). Even though an underestimation of 0.02 m was deemed negligible, given that uncertainty of Flight 3 at 95% is 0.083 m, and GCPFs will be used and highly recommended in future surveys.

5.2 Understanding patterns of morphological change

Rambla de la Viuda has been previously described as successive erosive-depositional sequences that repeated along the river channel (Calle et al. 2017). Although it is true that these sequences are present over river channels (Procter et al. 2010), the functioning of these sequences in Rambla de la Viuda is similar to the concept of discontinuous ephemeral streams (Bull 1997). In fact, the sequences usually end in lobe shaped bars (e.g.Calle et al. 2017; Calle et al. 2015; Hooke 2016; Lotsari et al. 2018; Sanchis-Ibor et al. 2017) that resemble 'channel fans' described in sheetflow areas by Bull (1997). These morphologies support a discontinuous distribution of the coarse sediment along the studied reach. The location in Fig. 6 constitutes an example of these sequences, with an upstream erosive segment (ES) and a downstream depositional segment (DS). Theoretically, dominant sediment transport patterns there should be determined by sediment supply associated to the catchment (Batalla et al. 2005) but also to valley morphology and smaller geometric features controlling the local reach hydraulics (Kondolf 1994b). However, the historical geomorphological evolution of the study reach provides evidence on the causes underlying current morphodynamic processes. In Calle et al. (2017) a good correlation between historic gravel mining extraction fronts and current depositional zones (with presence of lobe-shaped bars) was presented. Here, SfM-MVS was used to monitor one of this sequence. DoD showed that gravel accumulated predominantly inside the layout of the gravel pit during Flood #1, indicating refill of the accommodation space left by mining. Sediment infill was probably generated by the 220 m upstream retreat of the knickpoint generated by mining. It is true that change detection is not able to track the origin of the sediment and it could have come from upstream reaches. But the simplest explanation would be the closest upstream erosion segment, as it requires less energy. This evolution has been reported in many mined channels, but generally under perennial river regimes (Collins and Dunne 1990; Kondolf 1994a; Kondolf 1997; Martín-Vide et al. 2010; Rovira et al. 2005). On the contrary, Flood #2 produced an additional retreat of 185 m, but erosion and deposition were considerably lower. This may be due to the lack of accommodation space, sediment availability or perhaps grain size (Hooke 2016). How can Sfm-MVS help in exploring this different behavior?

5.3 SfM-MVS topographies and flood hydrographs

As previously discussed, changes occurred after two floods were properly registered by SfM-MVS. However, SfM-MVS may also go beyond this and give clues to the different behavior of reaches during flood events. Figure 6 demonstrates that fairly similar peak discharges (98 and 80, respectively) gave rise to very different geomorphological changes (see intensity colors in Fig. 6c). Different bedload transport associated to similar discharge is a common result of sediment load studies (Batalla et al. 2005). Nevertheless, this contradicts conclusions of some studies that directly relate flood frequency and sediment load (e.g. Downs et al. 2013). This source of controversy emerges with the complexity of sediment transport of rivers (Laronne and Reid 1993) and multiple variables that may influence the sediment transport (Hooke 2016). A possible interpretation is that differences in geomorphic work may be linked to a higher volume of stream flow (hm^3) and longer duration of effective discharge over entrainment thresholds (Batalla et al. 2005; Inbar 2012). Flood#1 accumulated 32.5 hm^3 and 24 days of flow and Flood #2 7.1 hm^3 and 11 days of flow. Thus total water volume decrease by 80% whereas peak discharges (98 and 80 m^3/s) only decreased by 20%. In the study section (Fig. 6) total mobilized sediment (deposit + erosion), decreased from 9600 m^3 in Flood #1 to 2671 m^3 in Flood #2 (a decrease of 72%) which is apparently congruent with total water volume decrease. Other hypothesis that may support this different behavior consists of sediment transport rates tends to be higher on the rising than on the falling limb of a flood hydrograph, as a result of sediment availability during the pre-flood period (Hassan and Church 2001; Mao 2012) producing a clockwise or positive hysteresis loop in the relationship between sediment transport and discharge (Walling and Webb 1988) which in turn may indicate low sediment availability (Mao et al. 2014). The longer duration of Flood #1 provided time-sustained geomorphic work during the recession limb of the flood, probably with a high selective particle entrainment due to the power of the receding stream flow. In terms of net bedload sediment transport, our results are interpreted as an anti-clockwise hysteresis effect in agreement with the morpho-dynamic modeling results during moderate flows in Rambla de la Viuda described by (Lotsari et al. 2018). However, these intra-event processes may be speculated, but cannot be discussed with certainty, through DoD analyses. This constitutes a limitation of 'change detection' with topographies and it would need additional field data before being able to discuss this in more depth. Other interpretations, e.g. entrainment thresholds, should be addressed by monitoring more flood events and include other variables, such sediment size or hydraulic parameters (Hooke 2016). In fact, SfM-MVS topographies could help in addressing the latter by using DEMs as geometrical boundary conditions for hydraulic modeling.

6 Conclusions

This paper applied SfM-MVS to reproduce riverbed topography in an ephemeral river channel. Different configuration of flight plans, camera settings, ground control points and workflows were tested to optimize its applicability in ephemeral rivers. 'Change detection' was used to show the potential application of repeated photogrammetric surveys to shed light onto morphological changes caused by flooding. These results were proved suitable for use as a base for further studies on river dynamics. Specific conclusions from this study are as follows:

1. The accuracy of SfM-MVS resulted in a limit of detection (LoD) of 0.190 and 0.198 m, appropriate for 'change detection' and DoD generation at reach scale. This fact was enhanced partially by the hydrological conditions, i.e. scant vegetation level and absence of water bodies.
2. High overlapping between photographs is recommended. An overlap index over 20 has been suggested for the survey to succeed. We therefore propose flight distribution at two heights (low and high) as the best solution for obtaining good DEM resolution when the speed of the flying platform is not fully customizable.
3. One of the most time consuming preprocessing tasks is deploying and measuring GCPs. Time can be reduced by fixing permanent targets on stable areas for use in georeferencing. A bias of 0.02 was detected in fixed targets. Even though this is negligible compared to the LoD, further investigation is needed to understand the source of this bias.
4. Change detection through SfM-MVS pointed out morphological changes produced by two bankfull floods. Topographic evolution of the study site revealed a erosive-depositional sequence similar to the one described by Bull (1997).
5. Detailed analysis of one of these sequences revealed that instream gravel mining is the principal driver for change. Sediment retention and knickpoint migration were related to the previous mining site.
6. Change detection also pointed out the different behavior of the study site during two floods of similar peak discharge. This appeared to be more closely related to the differences in the hydrograph duration and water volume during the recession limb. Larger topographic changes associated with longer flood duration were interpreted as indicative of sediment hysteresis. However, this conclusion needs further evaluation with additional monitoring and modeling of intra-event sediment transport and morphological changes.

Acknowledgements This paper has been funded by the Spanish Ministry of Economy and Competitiveness through the projects PALEOMED (CGL2014-58127-C3-1-R) and EPHIMED (CGL2017-86839-C3-1-R). MC funded by the Spanish FPI scholarship (BES-2012-056723), PA has received funding from the Academy of Finland, the Strategic Research Council (COMBAT project, Grant 293389). Special thanks to Alicia Castán for field support during flights and Laura Barrios for statistical support. Also to Patricia Mañana-Borrazas, Alejandro Güimil-Fariña, César Parcero-Oubiña and Pastor Fábrega-Álvarez for the course TDDG2016 and their help with PhotoScan software. I also thank the editor, Pedro Alfaro, and two unknown reviewers for kindly providing constructive comments and selflessly improve this paper.

References

Agisoft (2016a) Agisoft PhotoScan user manual. Professional edition, version 1.2. http://www.agisoft.com/pdf/photoscan-pro_1_2_en.pdf. Accessed 18 Mar 2016.

Agisoft (2016b) Agisoft PhotoScan professional edition. Version 1.2.6. http://www.agisoft.com/downloads/installer/. Accessed 18 Mar 2016.

Alho, P., Kukko, A., Hyyppä, H., Kaartinen, H., Hyyppä, J., & Jaakkola, A. (2009). Application of boat-based laser scanning for river survey. *Earth Surface Processes and Landforms, 34*(13), 1831–1838.

Alho, P., Vaaja, M., Kukko, A., Kasvi, E., Kurkela, M., Hyyppä, J., et al. (2011). Mobile laser scanning in fluvial geomorphology: mapping and change detection of point bars. *Zeitschrift für Geomorphologie Supplementary Issues, 55*(2), 31–50.

Anadón, P., & Moissenet, E. (1996). Neogene basins in the Eastern Iberian Range. In C. J. Dabrio & P. F. Friend (Eds.), *Tertiary basins of Spain: the stratigraphic record of crustal kinematics* (pp. 68–76). Cambridge: Cambridge University Press.

Batalla, R. J., Garcia, C., & Rovira, A. (2005). Chapter 8 A decade of sediment transport measurements in a large Mediterranean river (the Tordera, Catalan Ranges, NE Spain). *Developments in earth* *surface processes*, *7*, 117–140. https://doi.org/10.1016/S0928-2025(05)80014-8.

Boix-Fayos, C., Barberá, G. G., López-Bermúdez, F., & Castillo, V. M. (2007). Effects of check dams, reforestation and land-use changes on river channel morphology: case study of the Rogativa catchment (Murcia, Spain). *Geomorphology, 91*(1–2), 103–123.

Brasington, J., Rumsby, B. T., & McVey, R. A. (2000). Monitoring and modelling morphological change in a braided gravel-bed river using high resolution GPS-based survey. *Earth Surface Processes and Landforms, 25*(9), 973–990.

Brasington, J., Vericat, D., & Rychkov, I. (2012). Modeling river bed morphology, roughness, and surface sedimentology using high resolution terrestrial laser scanning. *Water Resources Research, 48*(11), W11519.

Bull, W. B. (1997). Discontinuous ephemeral streams. *Geomorphology, 19*(3–4), 227–276.

Calle, M., Alho, P., & Benito, G. (2017). Channel dynamics and geomorphic resilience in an ephemeral Mediterranean river affected by gravel mining. *Geomorphology, 285,* 333–346.

Calle, M., Lotsari, E., Kukko, A., Alho, P., Kaartinen, H., Rodriguez-Lloveras, X., et al. (2015). Morphodynamics of an ephemeral gravel-bed stream combining Mobile Laser Scanner, hydraulic simulations and geomorphological indicators. *Zeitschrift für Geomorphologie Supplementbände, 59*(3), 33–57.

Camarasa-Belmonte, A. M., & Segura-Beltrán, F. (2001). Flood events in Mediterranean ephemeral streams (ramblas) in Valencia region, Spain. *CATENA, 45*(3), 229–249.

Charlton, M. E., Large, A. R. G., & Fuller, I. C. (2003). Application of airborne LiDAR in river environments: The River Coquet Northumberland, UK. *Earth Surface Processes and Landforms, 28*(3), 299–306.

Collins, B., & Dunne, T. (1990) Fluvial geomorphology and river-gravel mining: a guide for planners, case studies included, issue 98. California Department of Conservation, Division of Mines and Geology. https://archive.org/details/fluvialgeomorpho98coll.

Doneus, M., Verhoeven, G., Fera, M., Briese, C., Kucera, M., & Neubauer, W. (2011). From deposit to point cloud—a study of low-cost computer vision approaches for the straightforward documentation of archaeological excavations. *Geoinformatics FCE CTU, 6,* 81–88.

Downs, P. W., Dusterhoff, S. R., & Sears, W. A. (2013). Reach-scale channel sensitivity to multiple human activities and natural events: Lower Santa Clara River California, USA. *Geomorphology, 189,* 121–134.

Dufour, S., Rinaldi, M., Piégay, H., & Michalon, A. (2015). How do river dynamics and human influences affect the landscape pattern of fluvial corridors? Lessons from the Magra River, Central-Northern Italy. *Landscape and Urban Planning, 134,* 107–118.

Ferreira, E., Chandler, J., Wackrow, R., & Shiono, K. (2017). Automated extraction of free surface topography using SfM-MVS photogrammetry. *Flow Measurement and Instrumentation, 54,* 243–249.

Flener, C., Vaaja, M., Jaakkola, A., Krooks, A., Kaartinen, H., Kukko, A., et al. (2013). Seamless mapping of river channels at high resolution using mobile LiDAR and UAV-Photography. *Remote Sensing, 5*(12), 6382–6407.

Fonstad, M. A., Dietrich, J. T., Courville, B. C., Jensen, J. L., & Carbonneau, P. E. (2013). Topographic structure from motion: a new development in photogrammetric measurement. *Earth Surface Processes and Landforms, 38*(4), 421–430.

Gallart, F., Cid, N., Latron, J., Llorens, P., Bonada, N., Jeuffroy, J., et al. (2017). TREHS: an open-access software tool for investigating and evaluating temporary river regimes as a first step for their ecological status assessment. *Science of the Total Environment, 607–608,* 519–540.

Gallart, F., Prat, N., García-Roger, E. M., Latron, J., Rieradevall, M., Llorens, P., et al. (2012). A novel approach to analysing the regimes of temporary streams in relation to their controls on the composition and structure of aquatic biota. *Hydrology Earth System Science, 16*(9), 3165–3182.

Hassan, M. A., & Church, M. (2001). Sensitivity of bed load transport in Harris Creek: Seasonal and spatial variation over a cobble-gravel bar. *Water Resources Research, 37*(3), 813–825.

Hooke, J. M. (2016). Morphological impacts of flow events of varying magnitude on ephemeral channels in a semiarid region. *Geomorphology, 252,* 128–143.

Inbar, M. (2012). Short-term channel changes after flash floods in the Upper Jordan River, Israel. *Horizons Geography, 79*(80), 26–36.

Javernick, L., Brasington, J., & Caruso, B. (2014). Modeling the topography of shallow braided rivers using Structure-from-Motion photogrammetry. *Geomorphology, 213,* 166–182.

Kasvi, E., Vaaja, M., Alho, P., Hyyppä, H., Hyyppä, J., Kaartinen, H., et al. (2013). Morphological changes on meander point bars associated with flow structure at different discharges. *Earth Surface Processes and Landforms, 38*(6), 577–590.

Knighton, D., 1998, Fluvial forms and processes: a new perspective, London, Arnold, Hodder Headline, PLC, xv + 383 pp. p.:

Kondolf, G. M. (1994a). Environmental planning in regulation and management of instream gravel mining in California. *Landscape and Urban Planning, 29*(2), 185–199.

Kondolf, G. M. (1994b). Geomorphic and environmental effects of instream gravel mining. *Landscape and Urban Planning, 28*(2), 225–243.

Kondolf, G. M. (1997). PROFILE: hungry water: effects of dams and gravel mining on river channels. *Environmental Management, 21*(4), 533–551.

Lane, S. N., Richards, K. S., & Chandler, J. H. (1994). Developments in monitoring and modelling small-scale river bed topography. *Earth Surface Processes and Landforms, 19*(4), 349–368.

Laronne, J. B., & Reid, L. (1993). Very high rates of bedload sediment transport by ephemeral desert rivers. *Nature, 366,* 148.

Lotsari, E. S., Calle, M., Benito, G., Kukko, A., Kaartinen, H., Hyyppä, J., et al. (2018). Topographical change caused by moderate and small floods in a gravel bed ephemeral river—A depth-averaged morphodynamic simulation approach. *Earth Surface Dynamics, 6*(1), 163–185.

Lotsari, E., Vaaja, M., Flener, C., Kaartinen, H., Kukko, A., Kasvi, E., et al. (2014). Annual bank and point bar morphodynamics of a meandering river determined by high-accuracy multitemporal laser scanning and flow data. *Water Resources Research, 50*(7), 5532–5559.

Lu, X. X., Zhang, S. R., Xie, S. P., & Ma, P. K. (2007). Rapid channel incision of the lower Pearl River (China) since the 1990s as a consequence of sediment depletion. *Hydrology Earth System Science, 11*(6), 1897–1906.

Luhmann, T., Robson, S., Kyle, S., et al. (2013). Close-range photogrammetry and 3D imaging. Berlin, Boston: De Gruyter. https://www.degruyter.com/view/product/203264. Accessed 06 July 2018.

Machado, M. J., Medialdea, A., Calle, M., Rico, M. T., Sánchez-Moya, Y., Sopeña, A., et al. (2017). Historical palaeohydrology and landscape resilience of a Mediterranean rambla (Castellón, NE Spain): Floods and people. *Quaternary Science Reviews, 171,* 182–198.

Mao, L. (2012) The effect of hydrographs on bed load transport and bed sediment spatial arrangement. *Journal of Geophysical Research Earth Surface*, *117*(F3), 1–16. https://doi.org/10.1029/2012JF002428.

Mao, L., Dell'Agnese, A., Huincache, C., Penna, D., Engel, M., Niedrist, G., et al. (2014). Bedload hysteresis in a glacier-fed mountain river. *Earth Surface Processes and Landforms, 39*(7), 964–976.

Marteau, B., Vericat, D., Gibbins, C., Batalla, R. J., & Green, D. R. (2017a). Application of structure-from-motion photogrammetry to river restoration. *Earth Surface Processes and Landforms, 42*(3), 503–515.

Marteau, B., Vericat, D., Gibbins, C., Batalla, R. J., & Green, D. R. (2017b). Application of structure-from-motion photogrammetry to river restoration. *Earth Surface Processes and Landforms, 42*(3), 503–515.

Martín-Vide, J. P., Ferrer-Boix, C., & Ollero, A. (2010). Incision due to gravel mining: Modeling a case study from the Gállego River, Spain. *Geomorphology, 117*(3–4), 261–271.

Muñoz-Narciso, E., Béjar, M., Tena, A., Vericat, D., Ramos, E., Brasington, J., Gibbins, C. N., & Batalla, R. J., Generación de modelos topográficos a partir de fotogrametria digital automatizada en un río de gravas altamente dinámico. in *Proceedings XIII Reunión nacional de geomorfología2014, Volume Avances de la Geomorfología en España 2012–2014*

Nouwakpo, S. K., Weltz, M. A., & McGwire, K. (2016). Assessing the performance of structure-from-motion photogrammetry and terrestrial LiDAR for reconstructing soil surface microtopography of naturally vegetated plots. *Earth Surface Processes and Landforms, 41*(3), 308–322.

Ollero, A., Ibisate, A., Granado, D., & de Asua, R. R. (2015). Channel responses to global change and local impacts: Perspectives and tools for floodplain management, Ebro river and Tributaries, NE Spain. In P. F. Hudson & H. Middelkoop (Eds.), *Geomorphic approaches to integrated floodplain management of lowland fluvial systems in North America and Europe: New York* (pp. 27–52). New York: Springer.

Procter, J. N., Cronin, S. J., Fuller, I. C., Lube, G., & Manville, V. (2010). Quantifying the geomorphic impacts of a lake-breakout lahar Mount Ruapehu, New Zealand. *Geology, 38*(1), 67–70.

Rinaldi, M., Wyżga, B., & Surian, N. (2005). Sediment mining in alluvial channels: Physical effects and management perspectives. *River Research and Applications, 21*(7), 805–828.

Rovira, A., Batalla, R. J., & Sala, M. (2005). Response of a river sediment budget after historical gravel mining (the lower Tordera, NE Spain). *River Research and Applications, 21*(7), 829–847.

Rychkov, I., Brasington, J., & Vericat, D. (2012). Computational and methodological aspects of terrestrial surface analysis based on point clouds. *Computers and Geosciences, 42,* 64–70.

Salas, R., & Casas, A. (1993). Crustal controls on the international architecture of sedimentary basins mesozoic extensional tectonics, stratigraphy and crustal evolution during the Alpine cycle of the eastern Iberian basin. *Tectonophysics, 228*(1), 33–55.

Sanchis-Ibor, C., Segura-Beltrán, F., & Almonacid-Caballer, J. (2017). Channel forms recovery in an ephemeral river after gravel mining (Palancia River, Eastern Spain). *CATENA, 158,* 357–370.

Simón, J. L., Pérez-Cueva, A. J., & Calvo-Cases, A. (2013). Tectonic beheading of fluvial valleys in the Maestrat grabens (eastern Spain): Insights into slip rates of Pleistocene extensional faults. *Tectonophysics, 593,* 73–84.

Singh, A. (1989). Review article digital change detection techniques using remotely-sensed data. *International Journal of Remote Sensing, 10*(6), 989–1003.

Skoulikidis, N. T., Sabater, S., Datry, T., Morais, M. M., Buffagni, A., Dörflinger, G., et al. (2017). Non-perennial Mediterranean rivers in Europe: Status, pressures, and challenges for research and management. *Science of The Total Environment, 577,* 1–18.

Smith, M. W., Carrivick, J. L., Hooke, J., & Kirkby, M. J. (2014). Reconstructing flash flood magnitudes using 'Structure-from-Motion': A rapid assessment tool. *Journal of Hydrology, 519,* 1914–1927.

Snavely, K. N. (2009). *Scene reconstruction and visualization from internet photo collections* (p. 169). Seattle, WA, USA: University of Washington. https://dl.acm.org/citation.cfm?id=2073240.

Stubbington, R., Chadd, R., Cid, N., Csabai, Z., Miliša, M., Morais, M., Munné, A., Pařil, P., Pešić, V., Tziortzis, I., Verdonschot, R. C. M., & Datry, T. (2018). Biomonitoring of intermittent rivers and ephemeral streams in Europe: Current practice and priorities to enhance ecological status assessments. *Science of The Total Environment*, *618*, 1096–1113.

Vaaja, M., Hyyppä, J., Kukko, A., Kaartinen, H., Hyyppä, H., & Alho, P. (2011). Mapping topography changes and elevation accuracies using a mobile laser scanner. *Remote Sensing, 3*(3), 587.

Verhoeven, G. (2011). Taking computer vision aloft – archaeological three-dimensional reconstructions from aerial photographs with photoscan. *Archaeological Prospection, 18*(1), 67–73.

Verhoeven, G., Doneus, N., Doneus, M., & Štuhec, S. (2015) From pixel to mesh: accurate and straightforward 3D documentation of cultural heritage from the Cres/Lošinj archipelago. in *Proceedings Istraživanja na otocima*, *vol 30, Hrvatsko arheološko društvo-Lošinjski muzej* (p. 165–176).

Vericat, D., Brasington, J., Wheaton, J., & Cowie, M. (2009a). Accuracy assessment of aerial photographs acquired using lighter-than-air blimps: Low-cost tools for mapping river corridors. *River Research and Applications, 25*(8), 985–1000.

Vericat, D., Vericat, J., Brasington, J., Wheaton, M., & Cowie, M. (2009b). Accuracy assessment of aerial photographs acquired using lighter-than-air blimps: low-cost tools for mapping river corridors. *River Research and Applications, 25*(8), 985–1000.

Walling, D. E., & Webb, B. W. (1988) The reliability of rating curve estimates of suspended sediment yield: some further comments. in *Proceedings Sediment Budgets. Proceedings of Porto Alegre Symposium*, Wallingford, UK, IAHS.

Westoby, M. J., Brasington, J., Glasser, N. F., Hambrey, M. J., & Reynolds, J. M. (2012). 'Structure-from-Motion' photogrammetry: A low-cost, effective tool for geoscience applications. *Geomorphology, 179,* 300–314.

Wheaton, J. M., Brasington, J., Darby, S. E., & Sear, D. A. (2010). Accounting for uncertainty in DEMs from repeat topographic surveys: improved sediment budgets. *Earth Surface Processes and Landforms, 35*(2), 136–156.

Affiliations

Mikel Calle[1] · **Petteri Alho**[2] · **Gerardo Benito**[1]

Mikel Calle
m.calle@mncn.csic.es

[1] National Museum of Natural Sciences, Spanish Research Council (CSIC), Calle de Serrano 115 BIS, 28006 Madrid, Spain

[2] Department of Geography and Geology, University of Turku/Turun Yliopisto, 20014 Turku, Finland